

# Isotopic evidence for an intensified hydrological cycle in the Indian sector of the Southern Ocean

Camille Hayatte Akhoudas (✉ [camille.akhoudas@geo.su.se](mailto:camille.akhoudas@geo.su.se))

Stockholm University

Jean-Baptiste Sallée

Sorbonne Université

Gilles Reverdin

Sorbonne Université

F. Alexander Haumann

Princeton University <https://orcid.org/0000-0002-8218-977X>

Etienne Pauthenet

IFREMER <https://orcid.org/0000-0002-0531-3810>

Christopher Chapman

CSIRO <https://orcid.org/0000-0002-0877-4778>

Félix Margirier

School of Earth and Atmospheric Sciences

Claire Lo Monaco

Sorbonne Université

Nicolas Metzl

Sorbonne Université

Julie Meilland

MARUM - University of Bremen <https://orcid.org/0000-0001-8966-3115>

Christian Stranne

Department of Geological Sciences, Stockholm University, Stockholm, Sweden <https://orcid.org/0000-0003-1004-5213>

---

## Article

### Keywords:

**Posted Date:** August 24th, 2022

**DOI:** <https://doi.org/10.21203/rs.3.rs-1952513/v1>

**License:**   This work is licensed under a Creative Commons Attribution 4.0 International License.

[Read Full License](#)



# Isotopic evidence for an intensified hydrological cycle in the Indian sector of the Southern Ocean

Camille Hayatte Akhoudas<sup>1,2\*</sup>, Jean-Baptiste Sallée<sup>3</sup>, Gilles Reverdin<sup>3</sup>, F. Alexander Haumann<sup>4</sup>, Etienne Pauthenet<sup>5</sup>, Christopher C. Chapman<sup>6</sup>, Félix Margirier<sup>7</sup>, Claire Lo Monaco<sup>3</sup>, Nicolas Metzger<sup>3</sup>, Julie Meilland<sup>8</sup>, and Christian Stranne<sup>1,2</sup>

<sup>1</sup>Department of Geological Sciences, Stockholm University, Stockholm, Sweden

<sup>2</sup>Bolin Centre for Climate Research, Stockholm University, Stockholm, Sweden

<sup>3</sup>CNRS/IRD/MNHN, LOCEAN, Sorbonne Université, Paris, France

<sup>4</sup>Atmospheric and Oceanic Sciences Program, Princeton University, Princeton, United States

<sup>5</sup>LOPS, IFREMER, Plouzané, France

<sup>6</sup>CSIRO, Hobart, Tasmania

<sup>7</sup>School of Earth and Atmospheric Sciences, Georgia Institute of Technology, Atlanta, United States

<sup>8</sup>MARUM, University of Bremen, Bremen, Germany

\*camille.akhoudas@geo.su.se

## ABSTRACT

The hydrological cycle is expected to intensify in a warming climate. However, observational evidence of such changes in the Southern Ocean is difficult to obtain due to sparse measurements and a complex superposition of changes in precipitation, sea ice, and glacial meltwater. We here disentangle these signals using a unique dataset of salinity and seawater oxygen isotope observations collected in the Indian sector of the Southern Ocean. Our results show that the atmospheric water cycle has intensified in this region between 1993 and 2021, increasing the salinity in subtropical surface waters by  $0.07 \text{ g kg}^{-1}$  per decade, and decreasing it in subpolar surface waters by  $-0.028 \text{ g kg}^{-1}$  per decade. In the subpolar region, this salinity decrease is countered by a salinity increase of  $0.008 \text{ g kg}^{-1}$  per decade from reduced sea ice melt, and enhanced by a salinity decrease of  $-0.005 \text{ g kg}^{-1}$  per decade from increased glacial melt. These changes extend the growing evidence for an acceleration of the atmospheric water cycle and a melting cryosphere that can be expected from global warming.

## Introduction

Over the past several decades, the Southern Ocean has experienced a complex array of hydrographic changes. These include large areas of the subpolar sector, south of the Antarctic Circumpolar Current (ACC), that have slightly cooled at the ocean surface<sup>1-5</sup>, contrasting with a marked warming north of the ACC extending from the surface to at least 1000 m<sup>4,6,7</sup>. The temperature changes are accompanied with a near-surface freshening in the subpolar Southern Ocean and extending at depth into the Antarctic intermediate waters<sup>5,8</sup>. These patterns of changes have important consequences for regional and global climate. The large warming north of the ACC indicates the capacity of the Southern Ocean to take up large amounts of excess

24 heat associated with climate change and to store it in intermediate layers, thereby buffering global atmospheric warming<sup>2,6,9</sup>.  
25 Changes in salinity mirror shifts in the water cycle that strengthen the static stability of the subpolar upper ocean, with  
26 consequences for the large-scale circulation<sup>10-12</sup>, sea ice regime<sup>13</sup>, and surface subpolar ocean cooling<sup>5,14,15</sup>. However, despite  
27 their widespread importance, the processes that cause changes in Southern Ocean temperature and salinity remain not fully  
28 understood. A number of studies have suggested that the widespread subpolar Southern Ocean surface freshening is consistent  
29 with an amplification of the global hydrological cycle associated with an increase in net precipitation at high latitudes<sup>6,16-18</sup>.  
30 Other studies have proposed different mechanisms including intensified freshwater flux from increased ice shelf and iceberg  
31 melting<sup>17,19,20</sup>, or from intensification of sea ice freshwater transport<sup>21</sup>. While climate models suggest that changes in Southern  
32 Ocean salinity over the past decades can be attributed in part to human-induced forcing<sup>6,22</sup>, these simulations are known  
33 to not include a realistic representation of changes in meltwater from Antarctic ice shelves, as well as having questionable  
34 representation of Antarctic sea ice cover and trends<sup>2,23-27</sup>.

35 In this paper, we explore long-term observations of seawater oxygen isotope and salinity in surface waters of the Indian  
36 sector (between 40°E and 90°E) of the Southern Ocean to document regional ocean changes, and explore potential causes of  
37 surface freshening. The observational data span over 28 years, from 1993 to 2021, leveraging both the *Océan Indien Service*  
38 *d'Observation (OISO)* French program that started in 1998<sup>28</sup> and which provides a regional sampling of surface salinity and  
39  $\delta^{18}\text{O}$  measurements (relative proportion of  $^{18}\text{O}$  to  $^{16}\text{O}$  referenced to Vienna Standard Mean Ocean Water); and additional  
40 hydrographic sections in the same sector of the Southern Ocean that span over the period 1993 to 1998. This dataset gives  
41 access to concurrent  $\delta^{18}\text{O}$  observations, allowing for the investigation of long-term changes in the freshwater sources that have  
42 distinct  $\delta^{18}\text{O}$  signatures. In the open ocean, away from the poles, the  $\delta^{18}\text{O}$  of surface waters is predominantly controlled by  
43 atmospheric processes (similar to surface salinity)—increasing from evaporation and decreasing from precipitation. At the  
44 poles, however,  $\delta^{18}\text{O}$  is also impacted by continental ice melt, which is very depleted in  $\delta^{18}\text{O}$ <sup>29</sup>, while salinity is impacted by  
45 both continental ice melt and sea ice formation and melt. As a result,  $\delta^{18}\text{O}$  is a useful tracer to differentiate freshwater signals  
46 coming from meteoric (precipitation, continental ice) or oceanic (sea ice) sources<sup>30-32</sup>.

## 47 Results

### 48 Regional surface trends

49 We compute the surface salinity- $\delta^{18}\text{O}$  relationship (Fig. 1d), and meridional sections of zonally averaged values from a set of  
50 observations sampled from 1993 to 2021, in the region corresponding to 40–90°E and 30–60°S. Since the mean circulation  
51 structure of the region is not zonal, we work in a streamwise coordinate system, calculating all means, anomalies, and associated  
52 trends in bins of constant mean dynamic topography, which we translate back to geographical space (pseudo-latitude,  $\tilde{lat}$ ) for  
53 readability purposes (see Methods). The zonally averaged meridional profiles of salinity and  $\delta^{18}\text{O}$  have similar shapes: higher  
54 salinity and  $\delta^{18}\text{O}$  north of  $\tilde{lat}$  46°S, and lower south of  $\tilde{lat}$  46°S (Fig. 1d; Fig. 2a,b). Within and northward the ACC (north of  
55  $\tilde{lat}$  46°S), the two properties actually follow a clear linear slope depending on the evaporation and precipitation characteristics  
56 of the region<sup>33</sup> (Fig. 1d). The salinity- $\delta^{18}\text{O}$  slope in this region is  $0.5 \pm 0.01$  ‰ g kg<sup>-1</sup>, typical of slopes found in mid-latitude  
57 oceans<sup>33</sup>. In contrast, south of  $\tilde{lat}$  46°S, the relationship between salinity and  $\delta^{18}\text{O}$  is much less clear (Fig. 1d) with small  
58 variations in salinity and comparatively much larger variability in  $\delta^{18}\text{O}$  (Fig. 1d). The large-scale meridional gradient of the  
59 isotopic composition of seawater is related to the gradual depletion in the  $\delta^{18}\text{O}$  of precipitation from the tropics toward higher

60 latitude that influence surface ocean  $\delta^{18}\text{O}$  (Supplementary Fig. 1).

61 Based on the zonally averaged meridional profiles, we define the local anomaly for each individual observation. Then, we  
62 investigate whether salinity and  $\delta^{18}\text{O}$  anomalies tend to co-vary. The two distinct regimes in the subtropical and in the subpolar  
63 sectors—also referred as the northern and the southern regions in the study—stand out clearly when computing correlation  
64 between salinity and  $\delta^{18}\text{O}$  anomalies. In the region north of  $\widetilde{\text{lat}}\ 46^\circ\text{S}$ , salinity and  $\delta^{18}\text{O}$  anomalies are strongly correlated  
65 (correlation coefficient mostly above 0.8; Fig. 2d). This high correlation is consistent with the observation of co-varying  
66 mean field (Fig. 1d), as a result of the two fields being controlled by the same processes, evaporation and precipitation,  
67 along a fixed mixing line i.e. the amount of salinity change for a given amount of  $\delta^{18}\text{O}$  change, set by local evaporation and  
68 precipitation characteristics<sup>34</sup>. Conversely, and still consistent with the mean fields, both parameters exhibit a substantially  
69 weaker relationship, inferred from low linear correlation coefficients, in the region south of  $\widetilde{\text{lat}}\ 46^\circ\text{S}$  (Fig. 2d). This poor  
70 correlation between anomalies of salinity and  $\delta^{18}\text{O}$  indicates that, in the southern region, the processes controlling salinity  
71 and  $\delta^{18}\text{O}$  are different. For example, while evaporation and precipitation have an impact on both parameters,  $\delta^{18}\text{O}$  is only  
72 marginally affected by sea ice formation and melt with a negligible fractionation factor on the order of 2‰<sup>35,36</sup>. However,  
73 changes in sea ice formation and melt mostly impact the surface salinity.

74 We now investigate long-term changes in salinity and  $\delta^{18}\text{O}$ . For this purpose, we first construct time series of annual  
75 medians of salinity and  $\delta^{18}\text{O}$  anomalies in the northern and southern regions (respectively north and south of  $\widetilde{\text{lat}}\ 46^\circ\text{S}$ ; Fig. 3).  
76 Robust long-term trends are found in both sectors. By fitting a weighed linear regression model (see Methods), we find that the  
77 northern region experienced an increase of both surface salinity (Fig. 3a) and  $\delta^{18}\text{O}$  (Fig. 3b) from 1993 to 2021. In contrast, in  
78 the southern region both surface salinity (Fig. 3c) and  $\delta^{18}\text{O}$  (Fig. 3d) decreased over the same period of time. In order to  
79 gain further insight in the meridional variability of the trend, we also compute long-term trends in the same  $\widetilde{\text{lat}}$  bins as Fig. 2.  
80 While we observe substantial variability along the meridional profile which is likely, at least partly, associated with observation  
81 limitations and uncertainties, the meridional profile of the trend clearly display two contrasting sectors on the northern and  
82 southern side of  $\widetilde{\text{lat}}\ 46^\circ\text{S}$  (Fig. 4). The magnitude is consistent with the trend computed in Fig. 3 (as represented by the grey  
83 shading in Fig. 4) with an increase of salinity and  $\delta^{18}\text{O}$  north of  $\widetilde{\text{lat}}\ 46^\circ\text{S}$  at rates of  $0.07 \pm 0.04\ \text{g kg}^{-1}$  per decade (Fig. 4a)  
84 and  $0.03 \pm 0.02\text{‰}$  per decade (Fig. 4b), respectively, and a decrease south of  $\widetilde{\text{lat}}\ 46^\circ\text{S}$  at rates of  $-0.02 \pm 0.01\ \text{g kg}^{-1}$  per  
85 decade (Fig. 4c) and  $-0.01 \pm 0.01\text{‰}$  per decade (Fig. 4d), respectively. While long-term trends of surface ocean  $\delta^{18}\text{O}$  in  
86 the Southern Ocean are limited to a small number of observations, trends in salinity can be investigated from a much larger  
87 dataset<sup>6,16,17,17–22</sup>. This offers the opportunity to test the robustness of the estimated salinity trends from our dataset, which is  
88 more limited in terms of number of observations. Trends of mixed layer characteristics have recently been reported from a  
89 large combined database for the period 1970–2018<sup>12</sup>. Their independent analysis reports similar upper ocean salinity changes  
90 compared with what we infer from our dataset, with a similar meridional pattern and consistent magnitude (Supplementary Note  
91 1). When looking at the spatial pattern from an independent analysis based on this much larger dataset, salinity changes are  
92 found to be mostly consistent along streamlines, which comfort our approach to investigate changes in streamwise coordinates  
93 (Supplementary Fig. 2).

## 94 Surface properties changes and associated forcing

95 The Southern Ocean is a data-sparse area making atmospheric reanalysis products generally the main tool for analysing  
96 observed surface ocean changes. However, there are inconsistencies among those products with a wide spread in precipitation  
97 minus evaporation (P-E) trends over the Southern Ocean (Supplementary Note 2), which would introduce uncertainties when  
98 interpreting surface salinity changes observed in the Indian sector of the Southern Ocean. This caveat is a motivation to apply  
99 an independent approach by estimating the P-E changes from ocean properties and surface flux estimates of sea ice and glacial  
100 meltwater (see Methods).

101 Qualitatively, long-term salinification in the subtropics can be explained by a decrease in P-E. In contrast, long-term  
102 freshening in the subpolar sector could be explained by an increasing P-E, a shift in sea ice regime, an increasing rate of ice  
103 sheet mass loss, or any combination of these. A strong correlation between salinity and  $\delta^{18}\text{O}$  in the subtropics (Fig. 2d) shows  
104 that the influence of sea ice on the salinity is limited to the southern region and does not considerably influence the northern  
105 region. In the subtropical sector, where all sea ice and glacial melt terms are set to 0, Eqs. 4 and 5 (see Methods) are used to  
106 quantify the plausible changes in P-E that could explain both the changes observed in salinity and  $\delta^{18}\text{O}$ . We compute the two  
107 equations by varying calculated trends and parameters within their estimated ranges, and select all consistent solutions across  
108 Eqs. 4 and 5. Our best estimate of changes in P-E resulting from this bootstrap exercise is a reduction of  $-75 \pm 23 \text{ mm yr}^{-1}$  per  
109 decade for precipitation with an isotopic composition of  $-7 \pm 2 \text{ ‰}$ . In the subpolar sector, we have more unknowns but we  
110 consider that long-term change in P-E is the most uncertain (Supplementary Note 2). So we attempt to estimate its contribution  
111 from surface ocean properties, sea ice and glacial melt flux changes over the last decades, based on a bootstrap exercise of Eqs.  
112 4 and 5. The isotopic signature of the Antarctic glacial meltwater is regionally variable ranging from  $\sim -20$  to  $\sim -40 \text{ ‰}$ <sup>29,37</sup>. The  
113 isotopic signature of precipitation is difficult to constrain but ranges from  $\sim -5$  to  $\sim -15 \text{ ‰}$  depending on latitude<sup>33,38</sup>. The  
114 isotopic signature of sea ice is much higher and has been better documented, ranging from  $\sim 0$  to  $\sim 2 \text{ ‰}$ <sup>39</sup>. We start by searching  
115 for solutions of Eqs. 4 and 5 assuming no changes have occurred in P-E, to test the hypothesis that observed changes could  
116 be solely driven by sea ice regime and glacial meltwater. No consistent solutions are found across Eqs. 4 and 5 under this  
117 assumption; so we conclude that changes in P-E must be involved in the observed surface ocean trends. Now, allowing for  
118 changes in P-E, and selecting all consistent solutions across Eqs. 4 and 5, we find that our best estimates of changes correspond  
119 to an increase of  $37 \pm 5 \text{ mm yr}^{-1}$  per decade for P-E, with  $\delta^{18}\text{O}$  of precipitation corresponding to  $-13 \pm 2 \text{ ‰}$ . In this solution  
120 we find an increase of  $6.5 \pm 3.5 \text{ mm yr}^{-1}$  per decade coming from glacial melt with a  $\delta^{18}\text{O}$  of  $-24 \pm 3 \text{ ‰}$ , and a decrease of sea  
121 ice melt of  $-12 \pm 4 \text{ mm yr}^{-1}$  per decade. An important result here is that ice sheet mass loss has a limited effect on salinity and  
122  $\delta^{18}\text{O}$  trends compared to P-E freshwater flux. Our computed equivalent salinity trend induced by P-E amounts to  $-0.028 \pm$   
123  $0.004 \text{ g kg}^{-1}$  per decade compensated by  $0.008 \pm 0.002 \text{ g kg}^{-1}$  per decade induced by sea ice and enhanced by  $-0.005 \pm 0.002$   
124  $\text{g kg}^{-1}$  per decade induced by glacial melt to sum up the total salinity trend observed in the subpolar sector. We note that we  
125 tested the extreme case where we assume that ice sheet mass loss had no impact on observed changes, and we are still able to  
126 find a plausible solution with a change in P-E freshwater flux slightly higher, corresponding to  $42 \pm 5 \text{ mm yr}^{-1}$  per decade.

127 The region south of  $\widetilde{\text{lat}} 52^\circ\text{S}$  covers much smaller amounts of data than further north (Fig. 2c) and is associated with a  
128 different magnitude of salinity and  $\delta^{18}\text{O}$  trends;  $-0.01 \pm 0.02 \text{ g kg}^{-1}$  per decade (Fig. 4a) and  $-0.06 \pm 0.04 \text{ ‰}$  per decade (Fig.  
129 4b), respectively. Even if these changes are computed in a shorter period of time, between 2001 and 2021 (Supplementary  
130 Fig. 7), the  $\delta^{18}\text{O}$  signal is considerably stronger. A significant decrease in  $\delta^{18}\text{O}$  coupled with a slight decrease in salinity is

131 consistent with a decline in sea ice melt (Supplementary Note 2) that is somewhat counteracting a higher decrease in salinity  
132 due to glacial meltwater and P-E increase.

## 133 Discussion

134 Long-term salinity observations in the Southern Ocean have revealed changes over the past decades, which are among the most  
135 pronounced in the global ocean<sup>6,8,16,18</sup>. However, the source of these changes has remained a conundrum. Salinity observations  
136 alone are not able to delineate the different elements involved in the freshwater cycle in the Southern Ocean. Here, in addition  
137 to salinity, we use  $\delta^{18}\text{O}$  observations and focus on surface water properties in the region of the Indian sector of the Southern  
138 Ocean between 1993 and 2021. We investigate the changes in two sectors, south and north of  $\widetilde{\text{lat}} 46^\circ\text{S}$ , which correspond  
139 approximately to the subantarctic front of the ACC, separating Antarctic Surface Waters in the south from Subtropical Surface  
140 Waters in the north. We attempt to minimize the aliasing of spatial variability by splitting measurements based on their respective  
141 dynamical region, as estimated by the climatological mean dynamic topography. We report a multidecadal salinification in  
142 the northern region of  $0.07 \pm 0.04 \text{ g kg}^{-1}$  per decade, associated with an increasing  $\delta^{18}\text{O}$  of  $0.03 \pm 0.02\text{‰}$  per decade from  
143 1993 to 2021. In contrast, the southern sector is freshened by  $-0.02 \pm 0.01 \text{ g kg}^{-1}$  per decade, and  $\delta^{18}\text{O}$  decreased at a rate  
144 of  $-0.01 \pm 0.01\text{‰}$  per decade from 1993 to 2021. These results are consistent with the latest IPCC report that assessed with  
145 high confidence that human-induced climate change has driven detectable changes in the global water cycle since the mid-20th  
146 century, with enhanced contrasts in P-E patterns over the oceans, which are projected to continue in a warmer world<sup>40</sup>. We  
147 demonstrate that the observed surface ocean changes result from an acceleration of the hydrological cycle between 1993 and  
148 2021, with a decrease in P-E of  $-75 \pm 23 \text{ mm yr}^{-1}$  per decade in the subtropical sector, contrasted by an increase in P-E of  $37 \pm$   
149  $5 \text{ mm yr}^{-1}$  per decade in the subpolar sector. Our multidecadal trend estimates are based on a mean isotopic composition  
150 of precipitation of  $-7 \pm 2\text{‰}$  in the northern sector and  $-13 \pm 2\text{‰}$  in the southern sector, consistent with previously reported  
151 estimates and their associated errors<sup>38</sup>.

152 It has been reported that the increased glacial meltwater input due to ice shelf thinning<sup>41,42</sup> and enhanced flux at the  
153 grounding line<sup>43</sup> mostly drive changes on the continental shelf<sup>5</sup>. We find that the enhanced glacial meltwater discharge from the  
154 Antarctic ice shelves only has a very limited influence (inducing a salinity trend of  $-0.005 \pm 0.002 \text{ g kg}^{-1}$  per decade of the total  
155 observed salinity change) on the open ocean salinity changes in the Indian sector of the Southern Ocean between 1993 and 2021.  
156 This result is consistent with Refs.<sup>5,17</sup>, stating that glacial freshwater flux increase is insufficient to explain the historical changes  
157 observed in the open ocean, away from the continental shelf. We note that as ice sheet mass loss is projected to continue in the  
158 future<sup>44</sup>, the signature on surface ocean salinity and  $\delta^{18}\text{O}$  might become more pronounced. In contrast, sea ice decline induces  
159 a positive salinity trend ( $0.008 \pm 0.002 \text{ g kg}^{-1}$  per decade) in the Indian sector of the Southern Ocean that is reduced by the  
160 negative trend induced by P-E ( $-0.028 \pm 0.004 \text{ g kg}^{-1}$  per decade), leading to a net surface ocean freshening. This feature is  
161 consistent with estimates from Ref<sup>21</sup> for this region, showing a decline in the northward sea ice transport in the Indian sector of  
162 the Southern Ocean and upstream of this region. The ocean's salinity response to this signal in a model<sup>5</sup> is a clear salinification,  
163 consistent with the slight negative salinity trend accompanied by the strong negative  $\delta^{18}\text{O}$  trend south of  $\widetilde{\text{lat}} 52^\circ\text{S}$ .

164 Our study quantifies the contribution of changes in freshwater forcing that influence surface water properties in the Southern  
165 Ocean directly from observations. The results have important implications. First, we demonstrate the strength of the *OISO*  
166 long-term monitoring program recording concomitantly  $\delta^{18}\text{O}$  and hydrographic properties to disentangle complex processes

167 currently at play in polar oceans. Second, our findings suggest only a limited influence of Antarctic ice discharge increases on  
 168 the surface water properties in the subpolar ocean, away from the continent. However, this signal may become more prominent<sup>23</sup>  
 169 in future, as the ice discharge is projected to accelerate<sup>45</sup>. Our approach and continued monitoring of these surface ocean  
 170 processes can be used as an early warning system to detect when and how ongoing ice sheet mass loss will start impacting  
 171 ocean characteristics and the associated circulation, with important consequences and feedback for the global climate, and the  
 172 ice sheet mass loss itself<sup>23,46,47</sup>. Third, providing a quantification of the role of forcings onto observed subpolar freshening  
 173 and subtropical salinification opens the door to better gauge the role of human activities on ocean characteristics, and offers a  
 174 framework and target for future climate model development to ensure that the critical processes in the polar regions are correctly  
 175 represented. We note that our results are only applicable to the investigated Indian sector of the Southern Ocean (40–90°E and  
 176 30–60°S). They should not be extrapolated to the wider Southern Ocean, since changes in surface freshwater fluxes and their  
 177 imprint on the ocean can have a spatially complex pattern, such as e.g. identified for sea ice changes<sup>5</sup>.

## 178 **Methods**

### 179 **Linking changes of freshwater forcing to changes of surface ocean properties**

To assess how the changing atmospheric freshwater flux affected the surface ocean properties in the Indian sector of the Southern Ocean, we compute a possible range of P-E changes from salinity,  $\delta^{18}\text{O}$  observed trends and the best estimate of glacial meltwater and sea ice changes. This approach enables us to overcome the inhomogeneities among reanalysis products (Supplementary Note 2). The salinity budget of the mixed layer<sup>48</sup> can be written as:

$$h \frac{dS}{dt} = FWF(S_{FWF} - S_0) + Entr + Diff, \quad (1)$$

where  $h$  is the depth of the mixed layer;  $S_0$  the mean mixed layer salinity;  $FWF$  is a water flux at the ocean surface with a salinity  $S_{FWF}$  in unit  $\text{m s}^{-1}$  (we will hereafter refer to freshwater fluxes as  $FWF$ , although we note that these fluxes can have a positive salinity  $S_{FWF}$ );  $Entr$  corresponds to the entrained salinity flux at the base of the mixed layer; and  $Diff$  is the diffusive salinity flux across the mixed layer boundary, which can involved either vertical or horizontal mixing. Integrating the salinity budget over an entire seasonal cycle, and assuming that entrainment and diffusion have not changed, the long-term salinity change  $\Delta S$  can be written as:

$$h\Delta S = (S_{FWF} - S_0)\Delta \int FWF, \quad (2)$$

where  $\int FWF$  is the integrated freshwater flux over one year, and  $\Delta \int FWF$  is its long-term change. Decomposing the freshwater component in P-E flux ( $\int FWF = F_{P-E}$ ), sea ice induced flux ( $\int FWF = F_{SI}$ ), and glacial meltwater flux ( $\int FWF = F_{IS}$ ) gives:

$$h\Delta S = (S_{P-E} - S_0)\Delta F_{P-E} + (S_{SI} - S_0)\Delta F_{SI} + (S_{IS} - S_0)\Delta F_{IS}, \quad (3)$$

which we can rewrite as:

$$\Delta F_{P-E} = \frac{h\Delta S - (S_{SI} - S_0)\Delta F_{SI} - (S_{IS} - S_0)\Delta F_{IS}}{(S_{P-E} - S_0)} \quad (4)$$

Repeating the same exercise but for a  $\delta^{18}\text{O}$  budget integrated over the mixed layer leads us similarly to:

$$\Delta F_{P-E} = \frac{h\Delta \delta^{18}\text{O} - (\delta^{18}\text{O}_{SI} - \delta^{18}\text{O}_0)\Delta F_{SI} - (\delta^{18}\text{O}_{IS} - \delta^{18}\text{O}_0)\Delta F_{IS}}{(\delta^{18}\text{O}_{P-E} - \delta^{18}\text{O}_0)} \quad (5)$$

180 In this paper, we use Eqs. 4 and 5 to determine long-term changes in P-E consistent with our best estimates of the other  
181 terms of the equations. We repeat the computation of Eqs. 4 and 5 50 000 times but varying all terms within their uncertainties,  
182 and we then select all solutions that provide consistent estimates of  $F_{P-E}$  when computed by Eq. 4 compared to when computed  
183 by Eq. 5 (within  $5 \text{ mm yr}^{-1}$  per decade of each other). The uncertainties in  $\Delta\delta^{18}\text{O}$  and  $\Delta S$  are inferred from the standard errors  
184 of the computed trends, and all other terms and associated uncertainties are summarized in Table 1.

### 185 Long-term $\delta^{18}\text{O}$ and salinity observations

186 In this study, we use surface observations of oxygen-18 isotopic composition ( $\delta^{18}\text{O}$ ) and salinity (expressed as absolute salinity  
187 following TEOS-10), from underway sampling at about 5–7 meters depth from sea surface and from stations sampling between  
188 0 and 50 meters depth, in the Indian sector of the Southern Ocean ( $40^\circ\text{E}$ – $90^\circ\text{E}$  and  $30^\circ\text{S}$ – $60^\circ\text{S}$ , Fig. 1a). These observations  
189 are from oceanographic research cruises undertaken during austral summer (December to February) from 1993 to 2021 (Fig.  
190 1b). Ship-based data used in this study are stored and distributed through the *OISO* database, for those sampled under the *OISO*  
191 program from 1998 to 2021<sup>28</sup>, and through the GISS (Goddard Institute for Space Studies) database for those from 1993 to  
192 1998<sup>33</sup>. All data flagged as "bad" or "probably bad" are discarded. Most of the observations were processed at the Laboratoire  
193 d'Océanographie et du Climat Expérimentations et Approches Numeriques (LOCEAN) in Paris, France. The seawater samples  
194 were analyzed using two different instrumental methods; (i) most data prior to 2010 were analyzed using isotope ratio mass  
195 spectrometry (Isoprime IRMS) coupled with a Multiprep system (dual inlet method), (ii) whereas most data since 2010 (and a  
196 few earlier data) were obtained by cavity ring down spectroscopy (CRDS) using a Picarro instrument (model L2130-i Isotopic  
197  $\text{H}_2\text{O}$ ) to measure for  $\delta^{18}\text{O}$ . Seawater samples were analyzed directly with the CRDS system using a stainless-steel liner from  
198 Picarro that is inserted in the injection port to avoid salt accumulation in the vaporizer. The use of a liner has the advantage of  
199 preserving the accuracy of the seawater isotope analyses as compared to direct injections into the vaporizer and the mesh traps  
200 about 80 % of the seawater salt<sup>49</sup>. Once the database was calibrated, it was then corrected for the analyzer-dependent "sea salt  
201 effect"<sup>49</sup>. The  $\delta^{18}\text{O}$  database is corrected so that deep water properties, which should be stable over the time period considered  
202 in this study, are constant across the different datasets. Typically, we focused over a range of neutral densities spanning over  
203  $28.15$  and  $28.3 \text{ kg m}^{-3} \gamma_n$  which corresponds to the old and stable Circumpolar Deep Water and encompasses water masses  
204 with typical time-scales of ventilation of the order of hundred years. This approach allowed us to correct for nonphysical offsets  
205 coming from different analytical techniques, different instruments and changes in standards.  $\delta^{18}\text{O}$  measurements uncertainty is  
206 on the order of  $0.06\text{‰}$  including instrumental and systematic errors associated with combining different datasets. In addition,  
207 we use concomitant salinity measurements from samples analyzed on a salinometer, calibrated CTD (Conductivity Temperature  
208 Depth) casts, and calibrated thermosalinograph data.

### 209 Streamwise coordinate system

210 In this study, all climatological means, associated anomalies, and trends are computed within dynamically consistent regions  
211 with regards to the mean position of fronts, in a streamwise coordinate system. Because the mean geostrophic circulation  
212 follows contours of constant mean dynamic topography, we chose to work in bins of constant mean dynamic topography<sup>50</sup>. In  
213 practice, all individual observations are ascribed a value of mean dynamic topography using the widely used product distributed  
214 by AVISO<sup>51</sup>. We then chose an irregular mean dynamic topography grid with bin size ranging from 0.1 to 0.3 m. Finer grids are  
215 used within the ACC since horizontal gradients of dynamic topography are larger there. Climatological means, anomalies, and

216 trends are all performed in this streamwise coordinate system. For readability purpose, the results are shown in latitude space,  
217 referred to pseudo latitude ( $\widetilde{lat}$ ), computed as the mean latitude in each mean dynamic topography bin (Fig. 1c).

### 218 **Trends and associated errors**

219 Trends are estimated by fitting linear regression models with their associated standard errors. The confidence level is established  
220 by computing the standard error of the regression. For trends performed in streamwise coordinate bins, we indicate trend values  
221 that are (i) less than half the computed standard errors, (ii) between half and one standard errors, (iii) between one and two  
222 standard errors, and (iv) more than two standard errors, to estimate the trend robustness with regards to the standard error.  
223 For trends produced in large sectors (north and south of  $\widetilde{lat}$  46°S), (i) we first compute local anomalies from the zonal-mean  
224 meridional profile by removing the mean of all observations in the streamwise coordinate bins; (ii) we then compute the annual  
225 25, 50, 75 percentiles of anomalies in the large sector; (iii) finally, we fit a weighted linear regression model to the annual  
226 medians, weighted by  $w = 1/IQR^2$ , where IQR is the interquartile range (percentile 75 minus percentile 25), which provides  
227 both an estimate of the long-term trend and its associated standard error.

### 228 **Changes in freshwater forcing in the Southern Ocean**

#### 229 **Sea ice**

230 The freshwater flux induced by the sea ice seasonal cycle and its interannual changes are obtained over the period 1993–2008  
231 from Ref.<sup>21</sup>, in which sea ice freshwater flux is obtained by combining sea ice concentration, drift and thickness, coupled with a  
232 mass balance approach to determine the volume divergence and local change in sea ice (see their methods section for further  
233 details). The sea ice freshwater flux trends inferred from these published estimates in our region of interest, between 40°E and  
234 90°E, is  $-31 \pm 6 \text{ mm yr}^{-1}$  per decade corresponding to the mean over the entire sector, i.e. it tends to increase surface ocean  
235 salinity. The mean sea ice freshwater flux trend over the latitude band we are considering as the subpolar sector in this study,  
236 between 60°S and 46°S, correspond to  $-12 \pm 4 \text{ mm yr}^{-1}$  per decade.

#### 237 **Ice sheet**

238 Continental ice meltwater changes can come from either increased ice discharge at the Antarctic grounding lines, or from ice  
239 shelf thinning. Here, we use the assessment of the latest IPCC report to estimate these two components<sup>44</sup>. In accordance with  
240 this assessment, the change in ice discharge is approximately equivalent to the change in mass balance. The Antarctic Ice Sheet  
241 mass loss rate was  $49 \pm 51 \text{ Gt yr}^{-1}$  from 1992 to 1999,  $70 \pm 59 \text{ Gt yr}^{-1}$  from 2000 to 2009, and  $148 \pm 54 \text{ Gt yr}^{-1}$  from 2010  
242 to 2016<sup>44</sup>. In consequence, assuming no change from 1992 to 1993, and that the rate of change was the same from 2016 to 2021  
243 as from 2005 to 2013 ( $10 \pm 14 \text{ Gt yr}^{-2}$ ), we infer that the ice discharge increased by a total of  $317 \pm 118 \text{ Gt yr}^{-1}$  from 1993 to  
244 2021, which translates into a mean acceleration of ice discharge corresponding to  $113 \pm 42 \text{ Gt yr}^{-1}$  per decade during this  
245 period. The latest IPCC assessment also reports estimates of basal melt related to ice shelf thinning with, however, substantial  
246 spatio-temporal variability<sup>42,44</sup>. They estimated an increase from  $1100 \pm 150 \text{ Gt yr}^{-1}$  to  $1570 \pm 140 \text{ Gt yr}^{-1}$  from the early  
247 1990s to the late 2000s, but a decrease from  $1570 \pm 140 \text{ Gt yr}^{-1}$  to  $1160 \pm 150 \text{ Gt yr}^{-1}$  in the late 2010s. The reconstruction of  
248 time-varying total glacial freshwater fluxes from the Antarctic Ice Sheet is a challenge when considering changes between the  
249 early 1990s and the early 2020s only, with evidence for significant interannual variability<sup>52</sup> and a reduction in melt rates in the  
250 last decade<sup>42</sup>. Based on these published results, we consider that the best estimates of plausible changes from 1993 to 2021 due  
251 to basal melt ranges between 20 and 200  $\text{Gt yr}^{-1}$  per decade. Our best estimates of changes in total (grounding line plus basal

252 melt fluxes) Antarctic glacial meltwater input therefore range from about 100 to 350 Gt yr<sup>-1</sup> per decade from 1993 to 2021.  
253 Assuming that this meltwater is evenly spread over the entire subpolar region (south of the mean dynamic topography contour  
254 of -0.2 m; corresponding to  $\widetilde{\text{lat}}$  46°S; area of  $\sim 3.5 \cdot 10^7$  km<sup>2</sup>), it converts into a freshwater flux trend ranging between 3 and 11  
255 mm yr<sup>-1</sup> per decade from 1993 to 2021. We note however that those changes in meltwater flux are likely not evenly spread over  
256 the entire subpolar region, but most likely have an impact to a greater extent in the coastal west Antarctic region than in the  
257 northern edge of the subpolar region of the Indian sector of the Southern Ocean. We therefore consider this rate of changes as  
258 an upper range estimate for the region considered in the present study.

### 259 **Precipitation and Evaporation**

260 As a result of the sparseness of *in situ* observations, atmospheric reanalyses have been widely used as a tool to report P-E over the  
261 Southern Ocean—the sign convention used here is that positive values of P-E refer to precipitation dominating over evaporation.  
262 However, long-term trends in P-E are highly uncertain due to the lack of measurements both spatially and temporally in the  
263 Southern Ocean in order to validate satellite products and modeled precipitation. Cautious use of reanalyses for climate change  
264 evaluation is thus needed as inhomogeneities between different products have been shown<sup>53</sup> and as we can observe between  
265 three different global atmospheric reanalysis products, ERA5<sup>54</sup>, JRA55<sup>55</sup> and GPCP coupled with OAFflux<sup>56,57</sup>, in our region  
266 of interest and at the circumpolar scale (Supplementary Note 2).

## 267 **References**

- 268 1. Armour, K. C., Marshall, J., Scott, J. R., Donohoe, A. & Newsom, E. R. Southern ocean warming delayed by circumpolar  
269 upwelling and equatorward transport. *Nat. Geosci.* **9**, 549–554 (2016).
- 270 2. Meredith, M. *et al.* Polar regions. chapter 3, ipcc special report on the ocean and cryosphere in a changing climate. (2019).
- 271 3. Purich, A. *et al.* Tropical pacific sst drivers of recent antarctic sea ice trends. *J. Clim.* **29**, 8931–8948 (2016).
- 272 4. Auger, M., Morrow, R., Kestenare, E., Sallée, J.-B. & Cowley, R. Southern ocean in-situ temperature trends over 25 years  
273 emerge from interannual variability. *Nat. communications* **12**, 1–9 (2021).
- 274 5. Haumann, F. A., Gruber, N. & Münnich, M. Sea-ice induced southern ocean subsurface warming and surface cooling in a  
275 warming climate. *AGU Adv.* **1**, e2019AV000132 (2020).
- 276 6. Swart, N. C., Gille, S. T., Fyfe, J. C. & Gillett, N. P. Recent southern ocean warming and freshening driven by greenhouse  
277 gas emissions and ozone depletion. *Nat. Geosci.* **11**, 836–841 (2018).
- 278 7. Gille, S. T. Decadal-scale temperature trends in the southern hemisphere ocean. *J. Clim.* **21**, 4749–4765 (2008).
- 279 8. Purich, A., England, M. H., Cai, W., Sullivan, A. & Durack, P. J. Impacts of broad-scale surface freshening of the southern  
280 ocean in a coupled climate model. *J. Clim.* **31**, 2613–2632 (2018).
- 281 9. Frölicher, T. L. *et al.* Dominance of the southern ocean in anthropogenic carbon and heat uptake in cmip5 models. *J. Clim.*  
282 **28**, 862–886 (2015).
- 283 10. Abernathey, R. P. *et al.* Water-mass transformation by sea ice in the upper branch of the southern ocean overturning. *Nat.*  
284 *Geosci.* **9**, 596–601 (2016).

- 285 **11.** Pellichero, V., Sallée, J.-B., Schmidtko, S., Roquet, F. & Charrassin, J.-B. The ocean mixed layer under southern ocean  
286 sea-ice: Seasonal cycle and forcing. *J. Geophys. Res. Ocean.* **122**, 1608–1633 (2017).
- 287 **12.** Sallée, J.-B. *et al.* Summertime increases in upper-ocean stratification and mixed-layer depth. *Nature* **591**, 592–598 (2021).
- 288 **13.** Goosse, H. & Zunz, V. Decadal trends in the antarctic sea ice extent ultimately controlled by ice–ocean feedback. *The*  
289 *Cryosphere* **8**, 453–470 (2014).
- 290 **14.** Kirkman IV, C. H. & Bitz, C. M. The effect of the sea ice freshwater flux on southern ocean temperatures in cesm3:  
291 Deep-ocean warming and delayed surface warming. *J. Clim.* **24**, 2224–2237 (2011).
- 292 **15.** Rye, C. D. *et al.* Antarctic glacial melt as a driver of recent southern ocean climate trends. *Geophys. Res. Lett.* **47**,  
293 e2019GL086892 (2020).
- 294 **16.** Durack, P. J., Wijffels, S. E. & Matear, R. J. Ocean salinities reveal strong global water cycle intensification during 1950 to  
295 2000. *science* **336**, 455–458 (2012).
- 296 **17.** Pauling, A. G., Bitz, C. M., Smith, I. J. & Langhorne, P. J. The response of the southern ocean and antarctic sea ice to  
297 freshwater from ice shelves in an earth system model. *J. Clim.* **29**, 1655–1672 (2016).
- 298 **18.** De Lavergne, C., Palter, J. B., Galbraith, E. D., Bernardello, R. & Marinov, I. Cessation of deep convection in the open  
299 southern ocean under anthropogenic climate change. *Nat. Clim. Chang.* **4**, 278–282 (2014).
- 300 **19.** Bintanja, R., Van Oldenborgh, G. & Katsman, C. The effect of increased fresh water from antarctic ice shelves on future  
301 trends in antarctic sea ice. *Annals Glaciol.* **56**, 120–126 (2015).
- 302 **20.** Swart, N. & Fyfe, J. The influence of recent antarctic ice sheet retreat on simulated sea ice area trends. *Geophys. Res. Lett.*  
303 **40**, 4328–4332 (2013).
- 304 **21.** Haumann, F. A., Gruber, N., Münnich, M., Frenger, I. & Kern, S. Sea-ice transport driving southern ocean salinity and its  
305 recent trends. *Nature* **537**, 89–92 (2016).
- 306 **22.** Hobbs, W. R., Roach, C., Roy, T., Sallée, J.-B. & Bindoff, N. Anthropogenic temperature and salinity changes in the  
307 southern ocean. *J. Clim.* **34**, 215–228 (2021).
- 308 **23.** Bronselaer, B. *et al.* Change in future climate due to antarctic meltwater. *Nature* **564**, 53–58 (2018).
- 309 **24.** Roach, L. A., Dean, S. M. & Renwick, J. A. Consistent biases in antarctic sea ice concentration simulated by climate  
310 models. *The Cryosphere* **12**, 365–383 (2018).
- 311 **25.** Roach, L. A. *et al.* Antarctic sea ice area in cmip6. *Geophys. Res. Lett.* **47**, e2019GL086729 (2020).
- 312 **26.** Holmes, C. R., Holland, P. R. & Bracegirdle, T. J. Compensating biases and a noteworthy success in the cmip5 representation  
313 of antarctic sea ice processes. *Geophys. Res. Lett.* **46**, 4299–4307 (2019).
- 314 **27.** Shu, Q., Song, Z. & Qiao, F. Assessment of sea ice simulations in the cmip5 models. *The Cryosphere* **9**, 399–409 (2015).
- 315 **28.** Reverdin, G. *et al.* The cise-locean seawater isotopic database (1998–2021). *Earth Syst. Sci. Data* **14**, 2721–2735 (2022).
- 316 **29.** Masson-Delmotte, V. *et al.* Information from paleoclimate archives. In *Climate change 2013: the physical science basis:*  
317 *Contribution of Working Group I to the Fifth Assessment Report of the Intergovernmental Panel on Climate Change*,  
318 383–464 (Cambridge University Press, 2013).

- 319 **30.** Craig, H., Gordon, L. I. *et al.* Deuterium and oxygen 18 variations in the ocean and the marine atmosphere. (1965).
- 320 **31.** Meredith, M. P. *et al.* The freshwater system west of the antarctic peninsula: spatial and temporal changes. *J. Clim.* **26**,  
321 1669–1684 (2013).
- 322 **32.** Meredith, M. P. *et al.* Changing distributions of sea ice melt and meteoric water west of the antarctic peninsula. *Deep. Sea*  
323 *Res. Part II: Top. Stud. Oceanogr.* **139**, 40–57 (2017).
- 324 **33.** LeGrande, A. N. & Schmidt, G. A. Global gridded data set of the oxygen isotopic composition in seawater. *Geophys.*  
325 *research letters* **33** (2006).
- 326 **34.** Schmidt, G. A. Error analysis of paleosalinity calculations. *Paleoceanography* **14**, 422–429 (1999).
- 327 **35.** Melling, H. & Moore, R. M. Modification of halocline source waters during freezing on the beaufort sea shelf: evidence  
328 from oxygen isotopes and dissolved nutrients. *Cont. Shelf Res.* **15**, 89–113 (1995).
- 329 **36.** Pfirman, S., Haxby, W., Eicken, H., Jeffries, M. & Bauch, D. Drifting arctic sea ice archives changes in ocean surface  
330 conditions. *Geophys. Res. Lett.* **31** (2004).
- 331 **37.** Akhoudas, C. *et al.* Ice shelf basal melt and influence on dense water outflow in the southern weddell sea. *J. Geophys. Res.*  
332 *Ocean.* **125**, e2019JC015710 (2020).
- 333 **38.** Nakamura, K., Aoki, S., Yoshimura, K. & Kurita, N. Distribution of oxygen isotope ratio of precipitation in the atlantic-indian  
334 sectors of the southern ocean. *Sola* **10**, 154–157 (2014).
- 335 **39.** Toyota, T. *et al.* Oxygen isotope fractionation during the freezing of sea water. *J. glaciology* **59**, 697–710 (2013).
- 336 **40.** H., D. *et al.* Water cycle changes. In *Climate Change 2021: The Physical Science Basis. Contribution of Working Group I*  
337 *to the Sixth Assessment Report of the Intergovernmental Panel on Climate Change*, 1055–1210 (Cambridge University  
338 Press, 2021).
- 339 **41.** Paolo, F. S., Fricker, H. A. & Padman, L. Volume loss from antarctic ice shelves is accelerating. *Science* **348**, 327–331  
340 (2015).
- 341 **42.** Adusumilli, S., Fricker, H. A., Medley, B., Padman, L. & Siegfried, M. R. Interannual variations in meltwater input to the  
342 southern ocean from antarctic ice shelves. *Nat. geoscience* **13**, 616–620 (2020).
- 343 **43.** Rignot, E. *et al.* Four decades of antarctic ice sheet mass balance from 1979–2017. *Proc. Natl. Acad. Sci.* **116**, 1095–1103  
344 (2019).
- 345 **44.** B., F.-K. *et al.* Ocean, cryosphere and sea level change. In *Climate Change 2021: The Physical Science Basis. Contribution*  
346 *of Working Group I to the Sixth Assessment Report of the Intergovernmental Panel on Climate Change*, 1211–1362  
347 (Cambridge University Press, 2021).
- 348 **45.** Seroussi, H. *et al.* Ismip6 antarctica: a multi-model ensemble of the antarctic ice sheet evolution over the 21st century. *The*  
349 *Cryosphere* **14**, 3033–3070 (2020).
- 350 **46.** Lago, V. & England, M. H. Projected slowdown of antarctic bottom water formation in response to amplified meltwater  
351 contributions. *J. Clim.* **32**, 6319–6335 (2019).
- 352 **47.** Golledge, N. R. *et al.* Global environmental consequences of twenty-first-century ice-sheet melt. *Nature* **566**, 65–72 (2019).

- 353 **48.** Ren, L., Speer, K. & Chassignet, E. P. The mixed layer salinity budget and sea ice in the southern ocean. *J. Geophys. Res.*  
354 *Ocean.* **116** (2011).
- 355 **49.** Benetti, M. *et al.* Inter-comparison of salt effect correction for  $\delta^{18}\text{O}$  and  $\delta^2\text{H}$  measurements in seawater by crds and irms  
356 using the gas-h<sub>2</sub>o equilibration method. *Mar. Chem.* **194**, 114–123 (2017).
- 357 **50.** Böning, C. W., Dispert, A., Visbeck, M., Rintoul, S. & Schwarzkopf, F. U. The response of the antarctic circumpolar  
358 current to recent climate change. *Nat. Geosci.* **1**, 864–869 (2008).
- 359 **51.** Rio, M., Mulet, S. & Picot, N. New global mean dynamic topography from a goce geoid model, altimeter measurements  
360 and oceanographic in-situ data. In *Proceedings of the ESA living planet symposium, Edinburgh* (2013).
- 361 **52.** Holland, P. R., Bracegirdle, T. J., Dutrieux, P., Jenkins, A. & Steig, E. J. West antarctic ice loss influenced by internal  
362 climate variability and anthropogenic forcing. *Nat. Geosci.* **12**, 718–724 (2019).
- 363 **53.** Bromwich, D. H., Nicolas, J. P. & Monaghan, A. J. An assessment of precipitation changes over antarctica and the southern  
364 ocean since 1989 in contemporary global reanalyses. *J. Clim.* **24**, 4189–4209 (2011).
- 365 **54.** Hersbach, H. *et al.* The era5 global reanalysis. *Q. J. Royal Meteorol. Soc.* **146**, 1999–2049 (2020).
- 366 **55.** Kobayashi, S. *et al.* The jra-55 reanalysis: General specifications and basic characteristics. *J. Meteorol. Soc. Jpn. Ser. II* **93**,  
367 5–48 (2015).
- 368 **56.** Huffman, G. J. *et al.* Global precipitation at one-degree daily resolution from multisatellite observations. *J. hydrometeorology*  
369 **2**, 36–50 (2001).
- 370 **57.** Yu, L. & Weller, R. A. Objectively analyzed air–sea heat fluxes for the global ice-free oceans (1981–2005). *Bull. Am.*  
371 *Meteorol. Soc.* **88**, 527–540 (2007).

## 372 **Acknowledgements**

373 This project has received funding from the European Research Council (ERC) under the European Union’s Horizon 2020  
374 research and innovation program (grant agreement 637770). FAH was supported by NSF’s Southern Ocean Carbon and Climate  
375 Observations and Modeling (SOCCOM, PLR-1425989) Project, and by NASA Grant 80NSSC19K1115. The authors gratefully  
376 thank the captain and the crew of the RV Marion Dufresne for their help in acquiring the long-term dataset as part of the *OISO*  
377 cruises and acknowledge INSU, IPEV and CNFH support for maintaining the *OISO* surveys. We also wish to acknowledge  
378 Catherine Pierre, Aïcha Naamar and Jérôme Demange for their skilled assistance in data analysis. The isotopic data were  
379 acquired at the L-CISE isotopic laboratory of OSU Ecce-Terra at LOCEAN, with support from OSU Ecce-Terra, LOCEAN and  
380 IPSL. This is a contribution to the LEFE Ker-Trend project.

## 381 **Author contributions statement**

382 CHA, JBS and GR directed the analysis of the datasets and share the responsibility for writing the manuscript with contributions  
383 from FAH, EP, CCC, FM, JM and CS. CLM and NM are the co-investigators of the ongoing *OISO* project, and produced the  
384 data synthesis with GR. All authors contributed to the final version of the manuscript.

## 385 **Data availability statement**

386 Datasets for this study are available in the in-text data citation references and the associated repositories:

387 The salinity and  $\delta^{18}\text{O}$  data by Refs.<sup>28,33</sup> (<https://www.seanoe.org/data/00600/71186/> and <https://data.giss.nasa.gov/o18data/>).

388 The salinity data by Ref.<sup>12</sup> (<https://github.com/jbsallee-ocean/GlobalMLDchange/tree/main/Databases>).

389 The sea ice freshwater flux data by Ref.<sup>21</sup> (<https://doi.org/10.16904/8>).

390 The AVISO sea-surface height data by Ref.<sup>51</sup> (<https://www.aviso.altimetry.fr/en/data/products/auxiliary-products/mdt.html>).

391 ERA5 monthly mean precipitation and evaporation rates by Ref.<sup>54</sup> (<https://cds.climate.copernicus.eu/cdsapp!/search?type=dataset>).

392 JRA55 monthly mean precipitation and evaporation rates by Ref.<sup>55</sup> (<https://rda.ucar.edu/>).

393 OAFlux monthly mean evaporation rate by Ref.<sup>57</sup> (<https://oafux.who.edu/>).

394 GPCP monthly mean precipitation rate by Ref.<sup>56</sup> (<https://www.ncei.noaa.gov/>).

395 GNIP yearly mean precipitation in Marion Island (<https://www.iaea.org/services/networks/gnip>).

**Table 1.** Estimated values and their uncertainties of the endmembers used in the system of equations to compute P-E flux trends. The mixed layer properties are estimated as the mean and standard deviation of the observations in the corresponding regions. Ranges of plausible values of the properties for the freshwater flux-related sources are based on literature<sup>29,33,37–39</sup>.

	North of $\widetilde{lat}$ 46°S (Subtropical)		South of $\widetilde{lat}$ 46°S (Subpolar)	
	Salinity (g kg <sup>-1</sup> )	$\delta^{18}\text{O}$ (‰)	Salinity (g kg <sup>-1</sup> )	$\delta^{18}\text{O}$ (‰)
mixed layer	35.20 ± 0.65	0.45 ± 0.33	33.95 ± 0.09	-0.26 ± 0.08
sea ice	–	–	4 ± 4	1 ± 1
ice sheet	–	–	0	-30 ± 10
precipitation	0	-5 ± 5	0	-10 ± 5

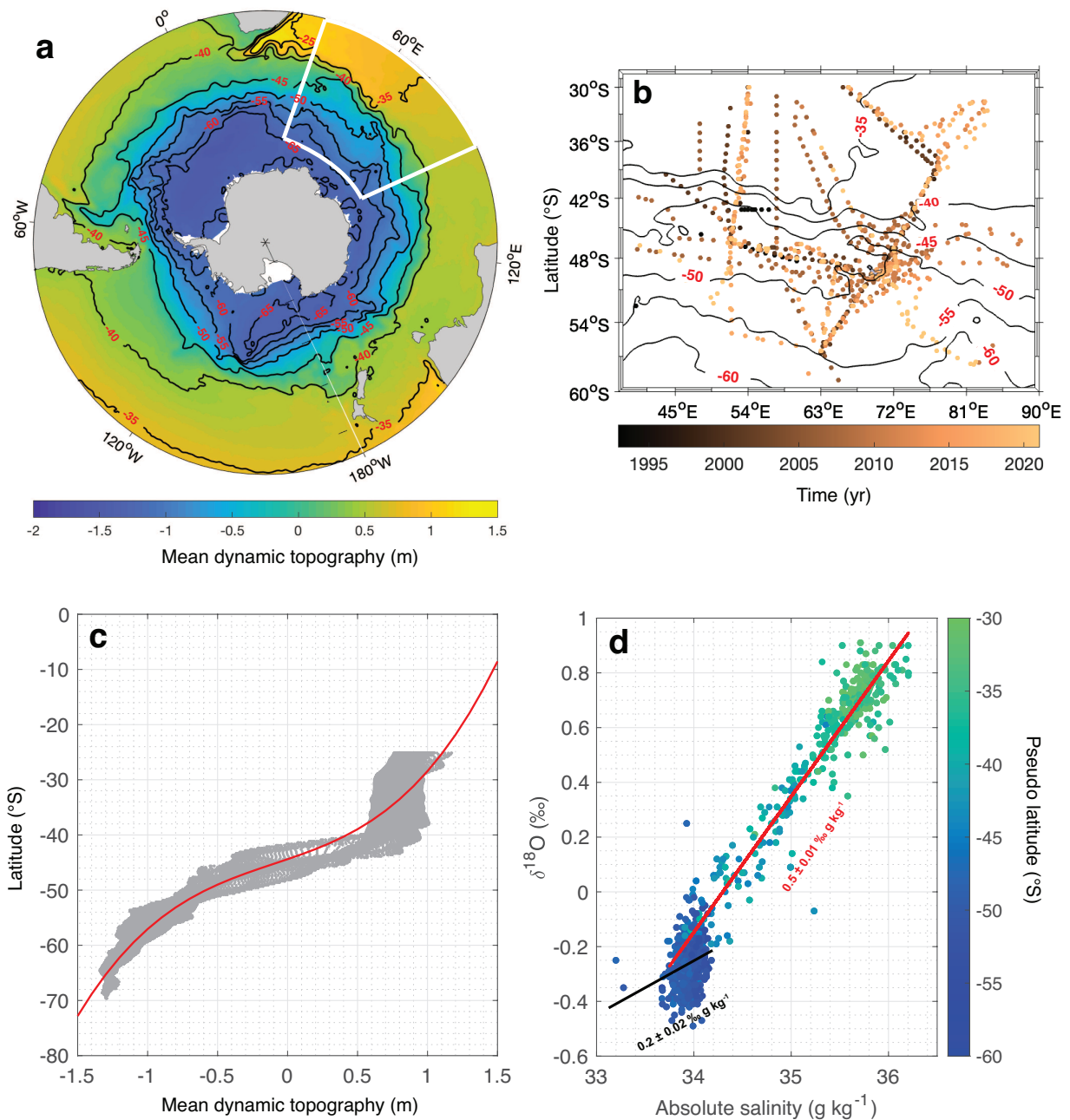


**Figure 1.** Mean dynamic topography<sup>51</sup> in color over the Southern Ocean (a). The white box represents the location of the ship-based observations obtained between 1993 and 2021 in color (b). Positions of the  $\widetilde{lat}$  contours are plotted as black lines and labelled in red on both maps. (c) Ensemble of the zonal-mean dynamic topography as a function of latitude in grey. The best-fit for the distribution corresponds to a third-order polynomial curve as shown by the red line. (d) Salinity- $\delta^{18}\text{O}$  diagram of surface observations with  $\widetilde{lat}$  in color. The salinity- $\delta^{18}\text{O}$  linear regression north of  $\widetilde{lat}$  46°S is shown as the red line (R-squared = 0.9) with its corresponding labelled slope— $0.5 \pm 0.01 \text{ ‰ g kg}^{-1}$ . The black line shows the poor linear correlation (R-squared = 0.2) between  $\delta^{18}\text{O}$  and salinity variables.

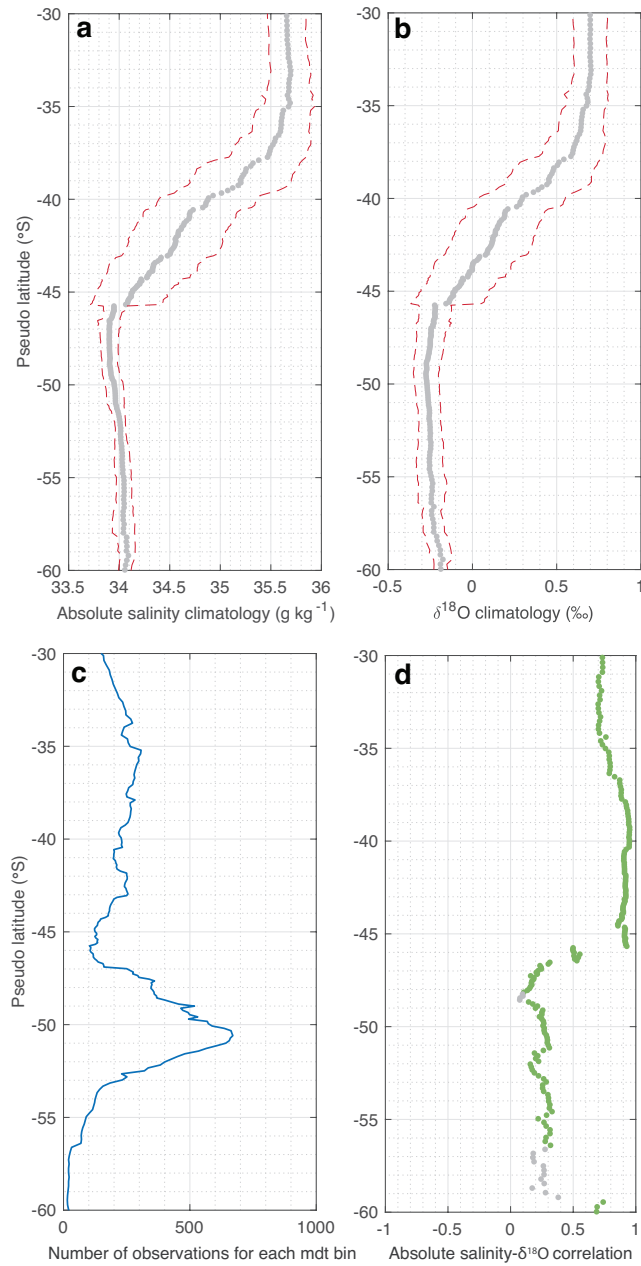


**Figure 2.** Meridional profiles of zonally averaged salinity (a) and  $\delta^{18}\text{O}$  (b) and their standard errors in red dashed lines. Number of surface salinity and  $\delta^{18}\text{O}$  observations per bins of  $\widetilde{\text{lat}}$  (c). Correlations between all salinity and  $\delta^{18}\text{O}$  observations in each bin of  $\widetilde{\text{lat}}$  (d). Green dots correspond to significant correlation between the two variables with a p-value  $\leq 0.05$ , conversely, grey dots are insignificant (p-value  $\geq 0.05$ ). Calculations are computed using an irregular mean dynamic topography grid with bin size ranging from 0.1 to 0.3 m.

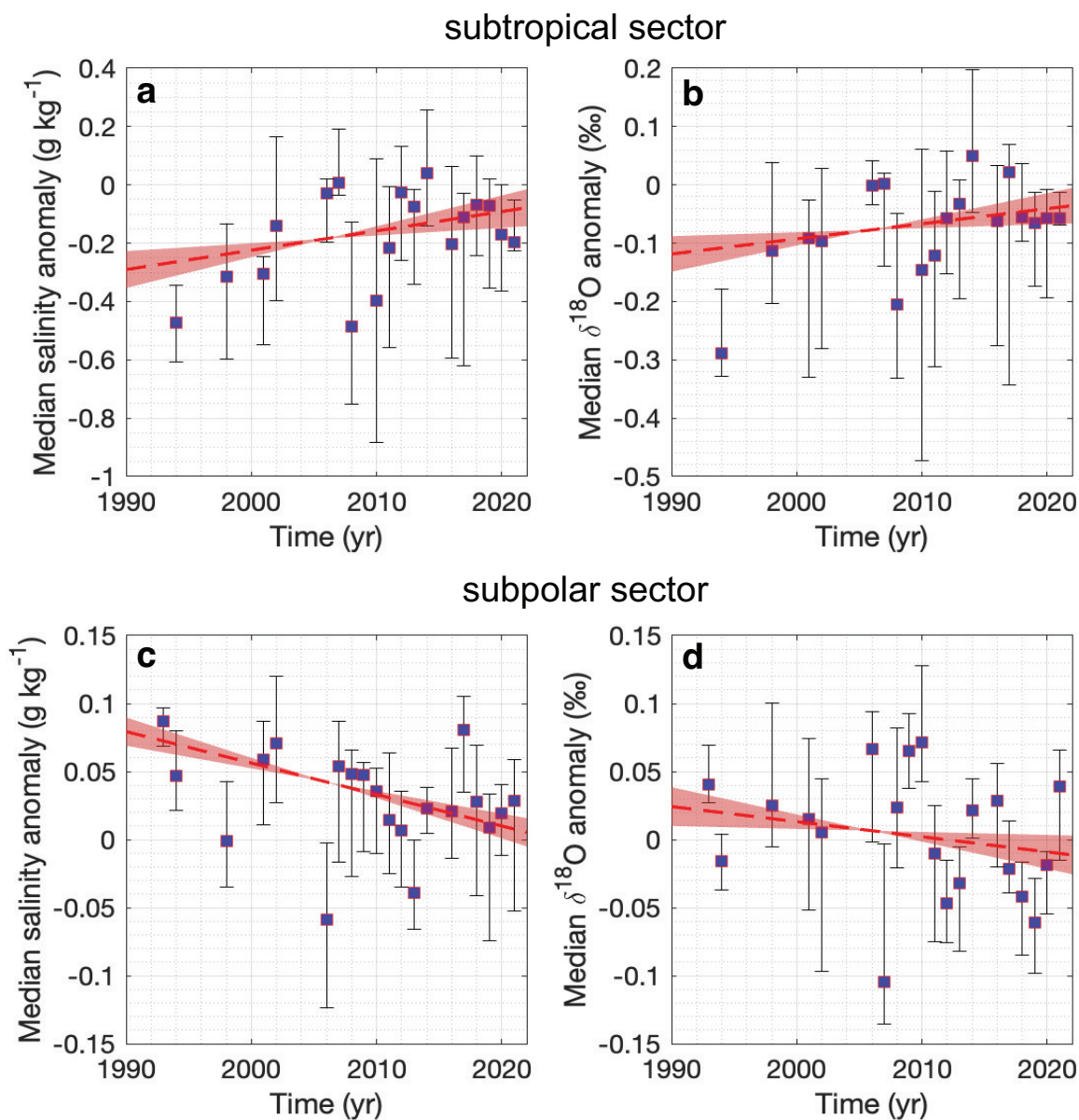


**Figure 3.** Median salinity (a and c) and  $\delta^{18}\text{O}$  (b and d) anomaly time series and associated trends for the subtropical (a and b) and subpolar (c and d) sectors. Each time series panel shows: the annual median anomaly (purple square from the regional salinity and  $\delta^{18}\text{O}$  climatology), computed for each individual observation; error bars shown in black referring to the 25th–75th percentile range; linear trends between 1993 and 2021 shown by the red dashed lines with their associated standard errors in red shading.

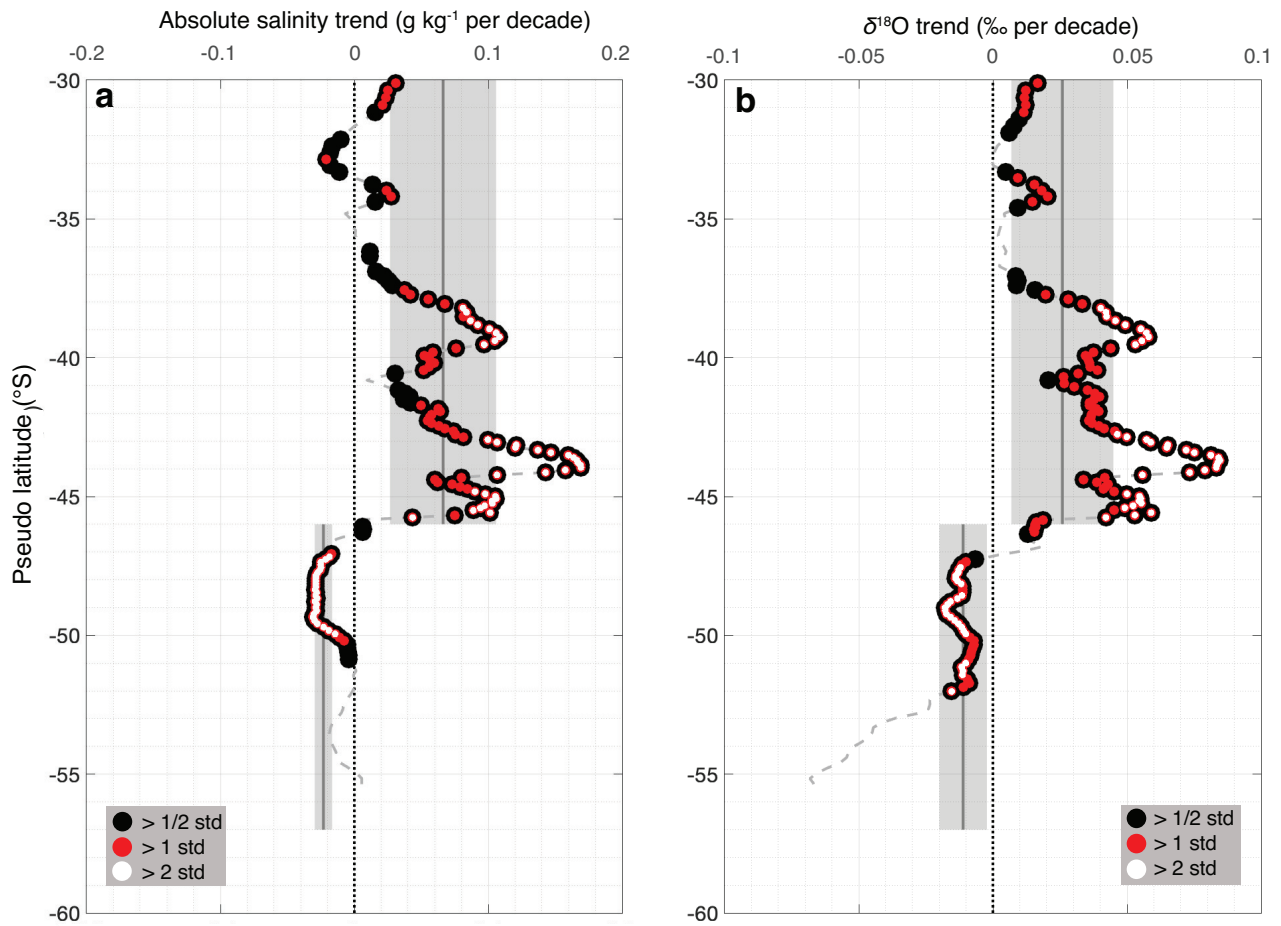


**Figure 4.** Meridional profiles of zonally averaged salinity (a) and  $\delta^{18}\text{O}$  (b) trends (grey dashed line). The black dots represent the trends larger than half their estimated standard errors, the red dots the trends larger than their estimated standard errors and white dots the trends larger than double their estimated standard errors. Trends are computed using an irregular mean dynamic topography grid with bin size ranging from 0.1 to 0.3 m. The grey line and shading show the mean and standard deviation of salinity and  $\delta^{18}\text{O}$  trends calculated from linear regression models in each region shown in Fig. 3.

## Supplementary Files

This is a list of supplementary files associated with this preprint. Click to download.

- [AkhoudasetalOISOSurfaceChangesSI.pdf](#)